# Gravity waves generated by the Hunga Tonga-Hunga Ha'apai volcanic eruption and their global propagation in the mesosphere lower thermosphere observed by meteor radars and modeled with the High-Altitude Mechanistic Circulation Model

Gunter Stober<sup>1</sup>, Sharon L. Vadas<sup>2</sup>, Erich Becker<sup>2</sup>, Alan Liu<sup>3</sup>, Alexander Kozlovsky<sup>4</sup>, Diego Janches<sup>5</sup>, Zishun Qiao<sup>3</sup>, Witali Krochin<sup>1</sup>, Guochun Shi<sup>1</sup>, Wen Yi<sup>6</sup>, Jie Zeng<sup>6</sup>, Peter Brown<sup>7,8</sup>, Denis Vida<sup>7</sup>, Neil Hindley<sup>24</sup>, Christoph Jacobi<sup>9</sup>, Damian Murphy<sup>10</sup>, Ricardo Burti<sup>11</sup>, Vania Andrioli<sup>12,13</sup>, Paulo Batista<sup>12</sup>, John Marino<sup>14</sup>, Scott Palo<sup>14</sup>, Denise Thorsen<sup>15</sup>, Masaki Tsutsumi<sup>16,17</sup>, Njål Gulbrandsen<sup>18</sup>, Satonori Nozawa<sup>19</sup>, Mark Lester<sup>20</sup>, Kathrin Baumgarten<sup>21</sup>, Johan Kero<sup>22</sup>, Evgenia Belova<sup>22</sup>, Nicholas Mitchell<sup>23,24</sup>, and Na Li<sup>25</sup>

Correspondence: gunter.stober@unibe.ch

<sup>&</sup>lt;sup>1</sup>Institute of Applied Physics & Oeschger Center for Climate Change Research, Microwave Physics, University of Bern, Bern, Switzerland

<sup>&</sup>lt;sup>2</sup>North West Research Associates (NWRA), Boulder, Colorado, USA

<sup>&</sup>lt;sup>3</sup>Center for Space and Atmospheric Research and Department of Physical Sciences, Embry-Riddle Aeronautical University, Daytona Beach, Florida, USA

<sup>&</sup>lt;sup>4</sup>Sodankylä Geophysical Observatory, University of Oulu, Finland

<sup>&</sup>lt;sup>5</sup>ITM Physics Laboratory, NASA Goddard Space Flight Center, Greenbelt, MD, USA

<sup>&</sup>lt;sup>6</sup>CAS Key Laboratory of Geospace Environment/CAS Center for Excellence in Comparative Planetology, Anhui Mengcheng Geophysics National Observation and Research Station, University of Science and Technology of China, Hefei, China

<sup>&</sup>lt;sup>7</sup>Dept. of Physics and Astronomy, University of Western Ontario, London, Ontario, Canada

<sup>&</sup>lt;sup>8</sup>Western Institute for Earth and Space Exploration, University of Western Ontario, London, Ontario, Canada

<sup>&</sup>lt;sup>9</sup>Institute for Meteorology, Leipzig University, Leipzig, Germany

<sup>&</sup>lt;sup>10</sup> Australian Antarctic Division, Kingston, Tasmania, Australia

<sup>&</sup>lt;sup>11</sup>Department of Physics, Federal University of Campina Grande, Campina Grande, Brazil

<sup>&</sup>lt;sup>12</sup>National Institute for Space Research (INPE), São José dos Campos, Brazil

<sup>&</sup>lt;sup>13</sup>China-Brazil Joint Laboratory for Space Weather, NSSC/INPE, São José dos Campos, Brazil

<sup>&</sup>lt;sup>14</sup>Colorado Center for Astrodynamics Research, University of Colorado Boulder, Boulder, CO, USA

<sup>&</sup>lt;sup>15</sup>University of Alaska, Fairbanks, USA

<sup>&</sup>lt;sup>16</sup>National Institute of Polar Research, Tachikawa, Japan

<sup>&</sup>lt;sup>17</sup>The Graduate University for Advanced Studies (SOKENDAI), Tokyo, Japan

<sup>&</sup>lt;sup>18</sup>Tromsø Geophysical Observatory, UiT - The Arctic University of Norway, Tromsø, Norway

<sup>&</sup>lt;sup>19</sup>Division for Ionospheric and Magnetospheric Research Institute for Space-Earth Environment Research, Nagoya University, Japan

<sup>&</sup>lt;sup>20</sup>University of Leicester, Leicester, UK

<sup>&</sup>lt;sup>21</sup>Fraunhofer Institute for Ceramic Technologies and Systems IKTS, Smart Ocean Technologies, Rostock, Germany

<sup>&</sup>lt;sup>22</sup>Swedish Institute of Space Physics (IRF), Kiruna, Sweden

<sup>&</sup>lt;sup>23</sup>British Antarctic Survey, Cambridge, CB3 0ET, UK

<sup>&</sup>lt;sup>24</sup>Department of Electronic and Electrical Engineering, University of Bath, Bath, UK

<sup>&</sup>lt;sup>25</sup>National Key Laboratory of Electromagnetic Environment, China Research Institute of Radiowave Propagation, Qingdao, China

**Abstract.** The Hunga Tonga-Hunga Haʻapai volcano erupted on 15 January 2022, launching Lamb waves and gravity waves into the atmosphere. In this study, we present results using 13 globally distributed meteor radars and identify the volcanic-caused gravity waves in the mesospheric/lower thermospheric winds. Leveraging the High-Altitude Mechanistic Circulation Model (HIAMCM), we compare the global propagation of these gravity waves. We found an eastward propagating gravity wave package with an observed phase speed of  $240\pm5.7$  m/s and a westward propagating gravity wave with an observed phase speed of  $166.5\pm6.4$  m/s. We identified these waves in the HIAMCM and obtained very good agreement of the observed phase velocities of  $239.5\pm4.3$  m/s and  $162.2\pm6.1$  m/s for the eastward and the westward wave, respectively. Furthermore, we estimate from meteor radar observations the eruption time to be within 6 minutes of the nominal value of 15th January 2022 04:15 UTC and localized the volcanic eruption to within 78 km relative to the WGS84 coordinate of the volcano.

10 Copyright statement. Creative Common 4.0 cc

# 1 Introduction

The Hunga Tonga-Hunga Ha'apai (HTHH) volcano erupted on 15 January 2022, with the strongest eruption occurring at 04:15 UTC. This eruption injected a gigantic amount of water vapor into the stratosphere and mesosphere (Millán et al., 2022), generated a huge ash plume reaching up to 57 km in altitude (Carr et al., 2022), and launched Lamb waves and gravity waves into the atmosphere (Wright et al., 2022; Liu et al., 2023; Vadas et al., 2023a). Because of the very large amplitudes involved, this eruption provided a unique opportunity to study the gravity wave propagation around the globe by a well-defined source event throughout all atmospheric layers from the troposphere to the thermosphere and ionosphere. Many previous studies focused on the Lamb wave generated by the sudden and vigorous explosion of the volcano in the Pacific (Wright et al., 2022; Matoza et al., 2022). TEC observations around the Pacific region indicated strong ionospheric disturbances associated with the Hunga-Tonga eruption (Themens et al., 2022; Heki, 2022; Yamada et al., 2022; Zhang et al., 2022). Recent modeling and observations indicate that these disturbances seemed to be the result of secondary wave generation rather than a direct propagation of the Lamb wave for which the mesosphere is an evanescent region due to the lower speed of sound (Vadas et al., 2023b; Stober et al., 2023). The more complicated propagation conditions at the mesosphere with the extremely cold mesopause and highly variable winds indicate why observations of the Hunga-Tunga eruption are underrepresented in the literature for this atmospheric layer. Wright et al. (2022) reported a signature of the Hunga-Tonga-caused waves above Hawaii seen in the airglow without a more detailed analysis. Meteor radar observations involving the Nordic Meteor Radar Custer and the Chilean Observation Network De Meteor Radars (CONDOR) indicated that the Lamb waves were attenuated at the MLT and the strongest amplitudes and signatures of the volcanic eruption were found by eastward and westward propagating gravity waves with an intrinsic phase speed of about 210 m/s and a horizontal wavelength of 1600-2000 km (Stober et al., 2023).

The importance of mesosphere/lower thermosphere (MLT) winds is understandable by the ExB-coupling (Miyoshi and Shinagawa, 2023; Shinbori et al., 2022). Multistep vertical coupling, which results from the dissipation of primary GWs from

HTHH in the thermosphere, is important for explaining why the volcanic-triggered waves have much higher phase velocities in TEC observations (Themens et al., 2022; Vadas et al., 2023b) and in MIGHTI neutral wind measurements in the thermosphere (Vadas et al., 2023a) as compared to the waves reported in the lower and middle atmosphere (Wright et al., 2022; Matoza et al., 2022; Stober et al., 2023). HTHH also provided a benchmark for the modeling of the volcanic-triggered gravity waves and their global propagation in a variable background wind field. Simulations with the Ground-to-Topside Model of Atmosphere and Ionosphere for Aeronomy (GAIA) and the Model for gravity wavE SOurce, Ray trAcing and reConstruction (MESORAC)/High Altitude Mechanistic Circulation Model (HIAMCM) demonstrated that concentric gravity wave structures generated by the HTHH eruption reached the thermosphere and caused perturbations in the neutral winds as well as in the TEC (Miyoshi and Shinagawa, 2023; Vadas et al., 2023b, a).

In this study, we investigate the mesospheric propagation of the strongest gravity waves launched by the HTHH eruption using globally distributed meteor radar observations covering the latitudes from 79°N on Svalbard to 78°S at McMurdo, Antarctica. In total, we identified the volcanic-induced gravity waves in wind measurements using 13 different meteor radars at various distances from the eruption site, which permits us to infer precisely the observed wave phase speeds for eastward and westward propagation. Furthermore, we demonstrate some asymmetries in the concentric gravity wave propagation, which led to characteristic amplitude variations at certain stations. Furthermore, we perform a similar analysis using HIAMCM wind data to compare the observational results with the model wind fields (Vadas et al., 2023a).

### 2 Meteor radar observations

Meteor radars have been used for decades to measure the winds and temperatures in the MLT (Hocking et al., 1997, 2001; Holdsworth et al., 2004; Meek et al., 2013). However, the HTHH eruption presented an opportunity to demonstrate the capabilities of the technique to detect and trace a gravity wave (GW) from a known source around the globe using a common and standardized analysis. The biggest challenge in processing the data from monostatic single station data is to achieve a temporal resolution of 10 min while still keeping a good altitude coverage of at least 10 km over the meteor layer. Considering the long vertical wavelength of the HTHH GW, we kept the frequently used vertical resolution of 2 km but with a 5-kilometer vertical averaging window centered around the respective altitude. A much longer temporal average than 10 minutes substantially attenuates the volcanic gravity wave signature and, thus, reduces the probability of identifying the HTHH GWs in the wind measurements.

We identified the HTHH GWs collecting data from 13 meteor radars around the globe. The meteor radars are located at Mc-Murdo (McM) (Marino et al., 2022), Davis (DAV), Rothera (ROT) (Dempsey et al., 2021), in Argentina the Southern Argentina Agile Meteor Radar (SAAMER) Tierra del Fuego (TDF) (Fritts et al., 2010), CONDOR represented by the Andes Lidar Observatory (ALO) (Stober et al., 2021b), Cariri (CAR) (Andrioli et al., 2013), Canadian Meteor Orbit Radar (CMOR) (in this study also - CMO) (Webster et al., 2004; Brown et al., 2010), Pokerflat (POK), Mengcheng (MEN) (Yang et al., 2023), Kunming (KUN) (Zeng et al., 2022), Svalbard (SVA) (Hall and Tsutsumi, 2020), the Nordic Meteor Radar Cluster (NORDIC)

- represented by the Tromsø meteor radar (TRO) (Hall and Tsutsumi, 2013) and Collm (COL) (Jacobi et al., 2007). All monostatic meteor radars were analyzed applying the retrieval algorithm including the World Geodetic Reference System (WGS84, (National Imagery and Mapping Agency, 2000)) to compute the East-North-Up coordinates at the geographic location of each detected meteor, a non-linear error propagation account for spatial and temporal wind shears within each time-altitude bin (Gudadze et al., 2019; Stober et al., 2021a). More details of the implementation are also found in Stober et al. (2021b, 2022). Figure 1 shows a map visualizing all meteor radar locations. The blue lines indicate the shortest great circle (GC) distance between each meteor radar and HTHH. The dashed red line indicates the full GC that connects ALO and HTHH. The yellow
  - between each meteor radar and HTHH. The dashed red line indicates the full GC that connects ALO and HTHH. The yellow line indicates the long GC path along the eastward direction connecting HTHH to the European radars. The lines indicate idealized propagation paths of the GWs launched by the eruption and are used to measure the distances. The distances shown in the map are computed at 90 km altitude to account for the mesospheric propagation.
- The meteor radars used in this study provide good coverage around the Pacific to investigate potential differences or asymmetries of the volcanic-triggered GW. Furthermore, four stations, namely MEN, KUN, ALO, and CAR are located very close to the same GC (dashed red line) and, thus, it is straightforward to reveal differences in the eastward and westward propagation of the GWs. A summary of all stations with their geographic coordinates and their eastward and westward GC distances to the HTHH eruption site are summarized in Table 1.

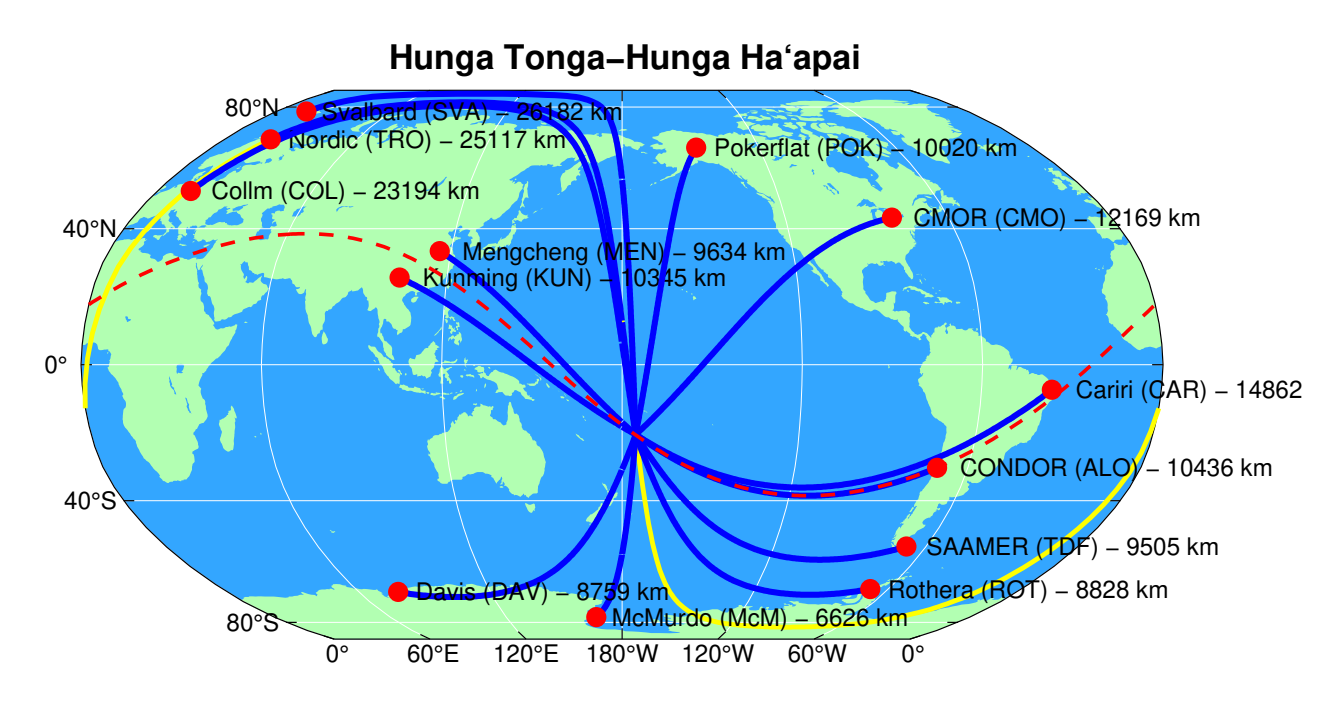


**Figure 1.** Robinson projection of the globe centered on the Pacific. The solid blue lines show the shortest GC distance between the volcanic eruption and the center of each station. The solid yellow line reflects the long GC path for the European radars. The dashed red line indicates the full GC path connecting the volcano and ALO, CAR, MEN, and KUN.

	longitude	latitude	GC (short) / km	GC (long) / km
McM (McMurdo)	166.72°E	77.85°S	6626 (W)	33404 (E)
DAV (Davis)	77.97°E	68.58°S	8759 (W)	31271 (E)
ROT (Rothera)	68.12°W	67.57°S	8828 (E)	31202 (W)
TDF (Tierra del Fuego)	67.75°W	53.79°S	9505 (E)	30525 (W)
MEN (Mengcheng)	116.0°E	33.4°N	9634 (W)	30398 (E)
KUN (Kunming)	103.0°E	25.6°N	10345 (W)	29685 (E)
ALO (CONDOR)	70.7°W	30.3°S	10436 (E)	29594 (W)
CAR (Cariri)	36.53°W	7.38°S	14862 (E)	25168 (W)
POK (Pokerflat, PFRR)	147.5°W	65.13°N	10020 (E)	30010 (W)
CMO (CMOR)	80.77°W	43.26°N	12169 (E)	27861 (W)
SVA (Svalbard)	15.99°E	78.17°N	13848 (W)	26182 (E)
TRO (Tromsø)	21.1°E	67.9°N	14913 (W)	25117 (E)
COL (Collm)	13.0°E	51.31°N	16836 (W)	23194 (E)

**Table 1.** Summary of the geographic locations for each meteor radar and GC distances relative to HTHH. The term short/long refers to the shortest/longest distance along the GC. The brackets after the GC distance indicate whether the westward or eastward HTHH GWs reached the station along this path.

# 0 3 HIAMCM global fields

The HIAMCM is a gravity wave-resolving GCM that has been used to study the generation of secondary waves above the Antarctic Peninsula and the Southern tip of the Andes (Becker and Vadas, 2018; Vadas and Becker, 2018). A more detailed description of the HIAMCM is found in Becker and Vadas (2020). Recently, it was demonstrated that the HIAMCM can be nudged to meteorological reanalysis such as The Modern-Era Retrospective Analysis for Research and Applications (MERRA-2). The nudging is implemented in the spectral domain, which permits specifying the large-scale background flow field providing realistic meteorological fields for the resolved gravity waves (Becker et al., 2022). Leveraging these new capabilities, the HTHH eruption and the corresponding gravity wave propagation were simulated with MESORAC and the HIAMCM and were analyzed to study the impact of the volcanic thermospheric-ionospheric system (Vadas et al., 2023b, a). Here, the MESORAC simulated the excitation, propagation, and dissipation of the local primary GWs created from the vertical updrafts of air in the stratosphere identified from GOES-17 satellite images. The local body forces and heatings created where the primary GWs dissipated were inputted into the HIAMCM, which subsequently generated the secondary GWs that propagated globally. In this study, we focus on the mesospheric data from the HIAMCM using the same model runs covering the altitude ranges between 80-100 km and with a temporal resolution of 5 minutes. The HIAMCM perturbations we show here are the results from the "Tonga run" (with inputs from MESORAC) minus that from the "base run" (without inputs from MESORAC). The HTHH GWs are extracted by subtracting a reference run from the disturbance simulation. Furthermore, we apply an observational filter for each meteor radar to account for the spatial and temporal sampling of these radars similar to previous studies (Pokhotelov et al., 2018; Stober et al., 2020, 2021c).

Figure 2 showcases global maps of how the HTHH secondary GWs propagated around the Earth at 4 different times for

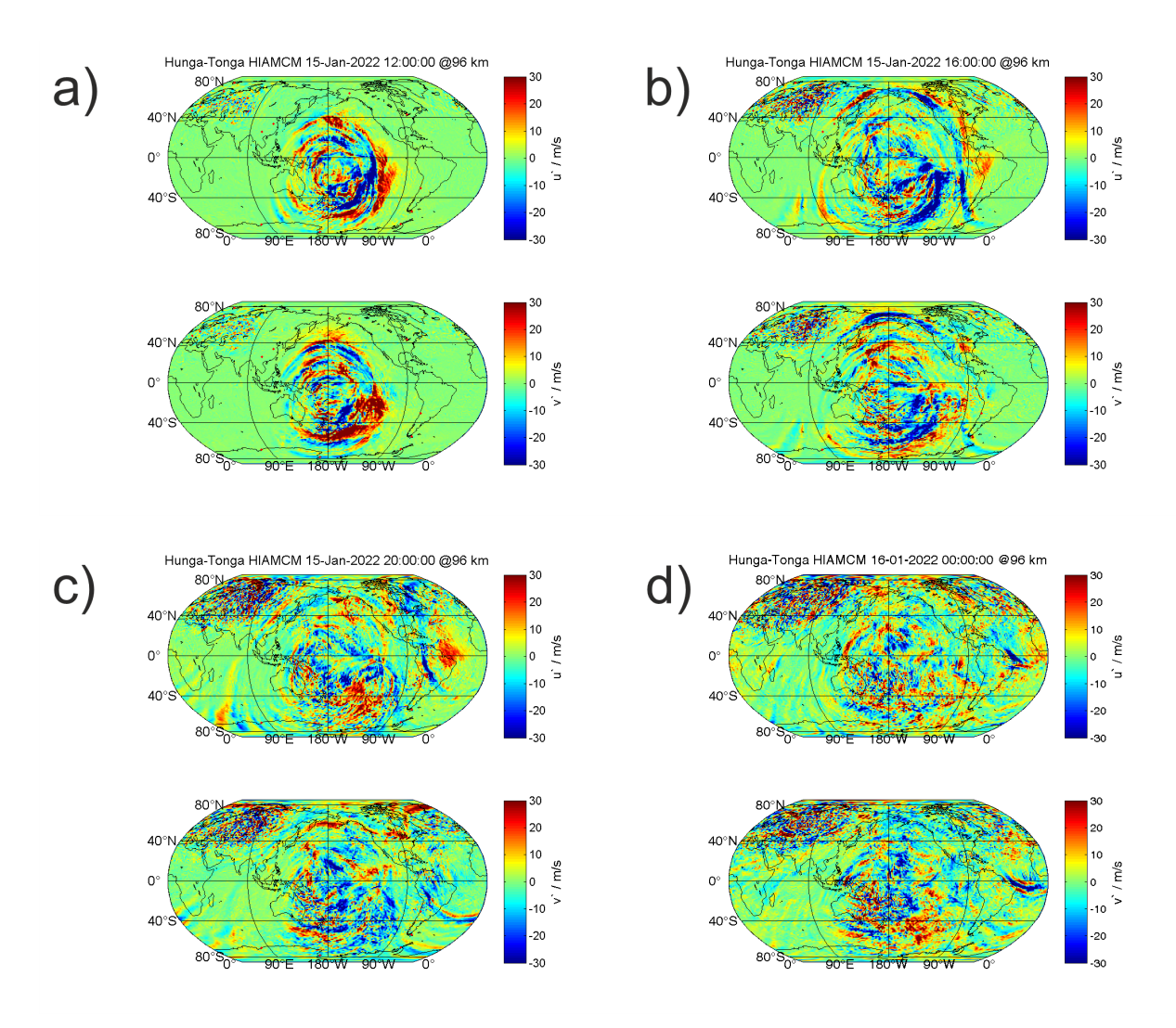


Figure 2. HIAMCM zonal (u') and meridional (v') wind fields from 15th January 2022 at 12, 16, 20, and 24 UT (a-d). The upper subpanel shows the zonal and the lower subpanel the meridional wind component.

the 15th of January (12 UT, 16 UT, 20 UT, 24 UT). The upper panels show the zonal and the lower panels the meridional wind, respectively. The HIAMCM GWs clearly propagate radially away from the HTHH eruption site. However, the model also reflects a substantial radial asymmetry in the gravity wave amplitudes indicating that the eruption sequence resulted in a substructure of the wavefronts for different azimuth directions. The largest amplitudes are found for the southeast propagation towards the Andes and the Antarctic Peninsula, whereas a much smaller GW amplitude was observable over Australia, China,

and the North American sector. This asymmetry is due to the wind filtering of the primary HTHH GWs in the lower-middle thermosphere, which created primarily northward-southward local body forces (i.e., horizontal accelerations) where they dissipated, as discussed in Vadas et al. (2023a). Such body forces do not excite secondary GWs perpendicular to the primary GW propagation direction, and therefore create an asymmetric distribution of secondary GWs (??).

In addition, some of the additional azimuthal GW asymmetries may be due to the complex eruption sequence (Vadas et al., 2023a). Results from the HIAMCM also show that the HTHH GWs traveling westward along the GC towards Europe are disturbed by the polar vortex in the northern hemisphere and, thus, almost no coherent wavefront arrives over Scandinavia, although this would have been the shortest distance to HTHH. However, the HIAMCM reveals that the most coherent wavefront from HTHH propagated towards South America and even gains strength over the Atlantic Ocean before reaching central Europe. This is consistent with the observations presented in (Stober et al., 2023).

## 4 HIAMCM and meteor radar

105

125

130

135

115 Tracking the HTHH secondary GWs around the globe from meteor radar wind observations requires identifying the GW package rather than one distinct feature that can be found in all observations. The main eruption lasted 3 hours and consisted of many vigorous detonations resulting in updrafts (Vadas et al., 2023a) triggering the HTHH primary GW field. The secondary GWs were generated by the local body forces created by the dissipation of the primary GWs n the mesosphere and thermosphere. Considering the HIAMCM simulation of the HTHH GW package underlines that there is a huge diversity of possible amplitudes and shapes of the GW package depending on the different GC paths the waves are propagating. Furthermore, derived phase velocities will depend on the ability to detect the edge of the HTHH GW package to pick the correct arrival time in the observation volume rather than on the maximum amplitude, which often corresponds more to the center of the eruption sequence. Thus, the time picks are prone to large uncertainties that have to be considered in the further analysis of HTHH GWs.

In the following, we briefly outline the analysis procedure. We examined the 10 min resolution meteor radar winds and subtracted a 4-hour running window to remove all large-scale waves such as planetary waves (mostly Quasi-2-Day-Wave (Q2DW) in the southern hemisphere), atmospheric tides, and GWs with observed periods longer than 4 hours. The vertically integrated anomalies were then inspected to identify the HTHH GW package by searching for peaks in the zonal, meridional, and horizontal winds. Our observations can be grouped into three different classes depending on the shape of the GW package, the amplitude, or a superposition with other waves. The timing was then estimated for all stations that showed a sinusoidal wave by the first onset of the GW. Typical examples of such stations are ALO, POK, and TDF. For the other cases, we searched for the first peak in an interval around the estimated arrival time e.g., CMOR, McM, and DAV.

Figure 3 compares the theoretical arrival times for all meteor radars (left column) and corresponding HIAMCM winds (right column) from the Antarctic Peninsula to Alaska. The cyan vertical lines indicate the arrival times of the eastward propagating HTHH GW package estimated from the best fit using all stations that detected this wave, whereas the black vertical lines reflect the best fit time of the westward wave. The dashed vertical red lines show the one sigma environment of the time picks for each

station. The y-axis for the HIMACM winds is reduced by a factor of 4 to compensate for the smaller amplitudes in the model. The observations as well as the HIAMCM reflect a remarkable agreement for several stations of the timing and wave pattern at ALO, POK, or CAR. Only CMOR exhibits a visible difference in the arrival time compared to HIAMCM. Although, CMOR is one of the most powerful systems used in this study, the HTHH GW is barely identifiable in the zonal wind component. Apparently, the observations indicate a much less clear wavefront and an earlier arrival time compared to the model and in relation to the other stations.

The comparison of the wind anomalies of the Antarctic stations of McM and DAV and the two radars located in China (MEN and KUN) are presented in Figure 4. Although the two meteor radars on the Antarctic continent are located at the closest distance to HTHH, the GW signature is barely visible in the data. The HTHH GW is mainly identified by a coherent sinusoidal signature (between the vertical lines), which was also found in other stations. However, the amplitude of this wave signature does not exceed the background atmospheric signal for these two stations. Furthermore, these two stations also reflect the largest discrepancy in the arrival time between the observations and HIAMCM. Interestingly, KUN and MEN meteor radars observed the HTHH GW with a much smaller amplitude than the counterparts eastward of the volcano in South America, although ALO, MEN, KUN, and CAR are almost on the same GC. The increased variability in the wind anomalies prior to the HTHH in the meteor radar data is mainly due to the diurnal variation in the meteor count rate, which reached a minimum during these times. This provides observational confirmation of the asymmetric azimuthal propagation that was found in the global HIAMCM zonal and meridional winds. Another important aspect is that the zonal and meridional winds are out of phase for MEN and KUN stations indicating a northwestward propagation, whereas CAR and ALO exhibit an in-phase relationship between the two wind components, which is expected because these GWs are eastward propagating. Also, the arrival times between the HIAMCM and the Chinese meteor radars are in much better agreement compared to McM and DAV.

Wind anomalies above the European sector are shown in Figure 5. We identified the eastward propagating gravity (long GC path) by searching for identical patterns in the wind anomalies for all three stations. Indicated by the cyan vertical lines a coherent wave structure exhibits an in-phase behavior of the zonal and meridional winds (as expected since the GWs are propagating northeastward), similar to what was found for the South American stations but with a 180 degree phase shift. HIAMCM winds also show some remnants of the eastward HTHH GW. However, the data is much noisier in the northern hemisphere winter due to the simulation of GWs from orographic forcing and the polar vortex. The increased variability in the observations may be due to the generation of GWs created by the breaking of the Lamb wave that arrived a few hours before the HTHH GWs (Stober et al., 2023). In addition, we note that Lamb waves create a continuum of GWs where they seed GWs at z 110 km (Vadas et al., 2023b).

# 5 Gravity wave observed phase speeds

150

155

160

165

Gravity wave phase speeds are derived from all meteor radar stations using the time picks for each individual station. The phase speeds are determined by fitting a distance vs. time and time vs distance to account for errors in the time picks as well as for the size of the observations volume. We assumed a 3-hour uncertainty for the time corresponding to the most active part

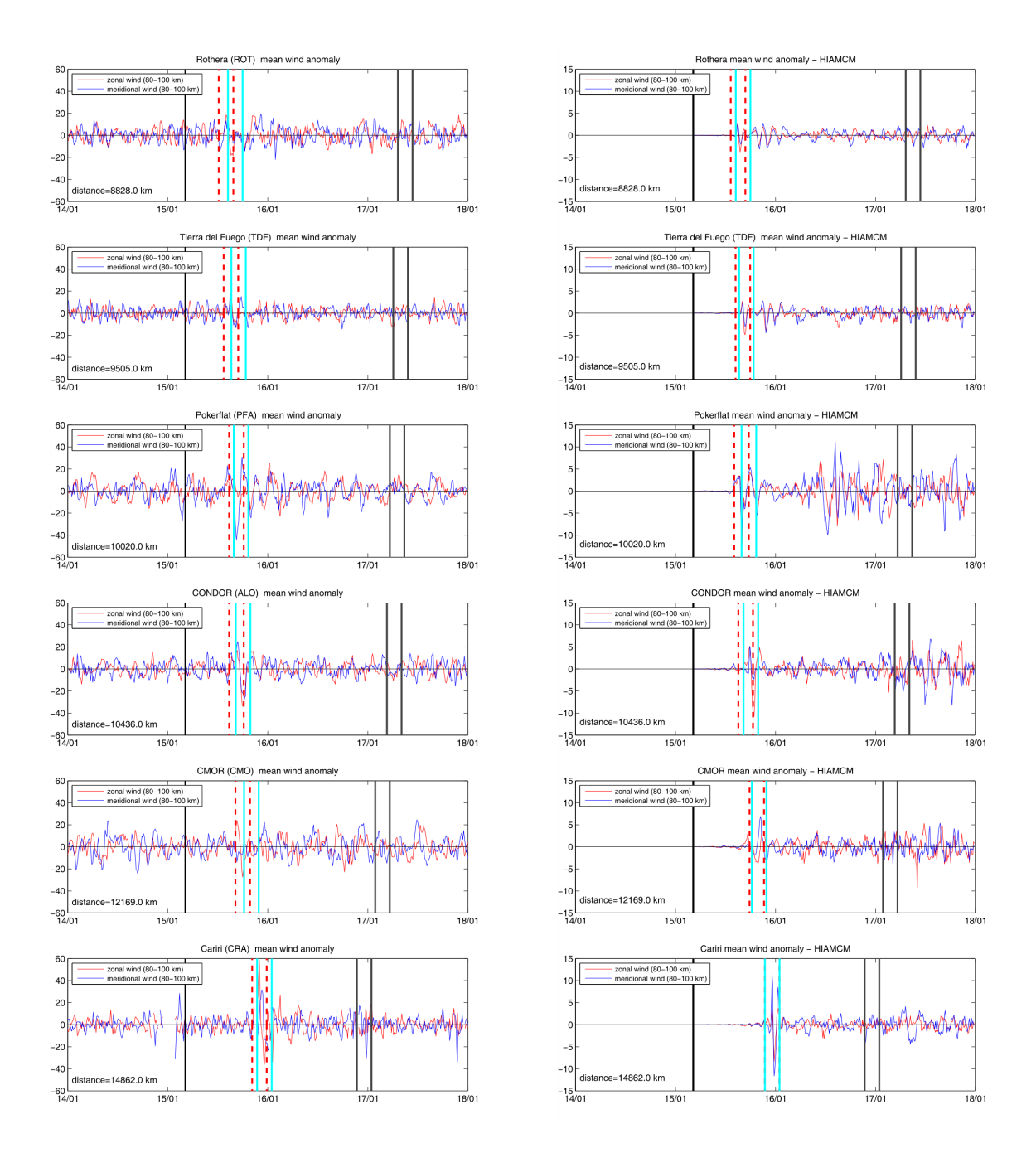


**Figure 3.** Wind anomalies for the meteor radars located eastward of HTHH and corresponding anomalies from HIAMCM. The cyan vertical lines embrace the predicted arrival of the eastward propagating GW. The black vertical lines indicate the timing for the westward propagating HTHH GW package. The dashed vertical lines indicate the one-sigma interval of the time picks for each station.

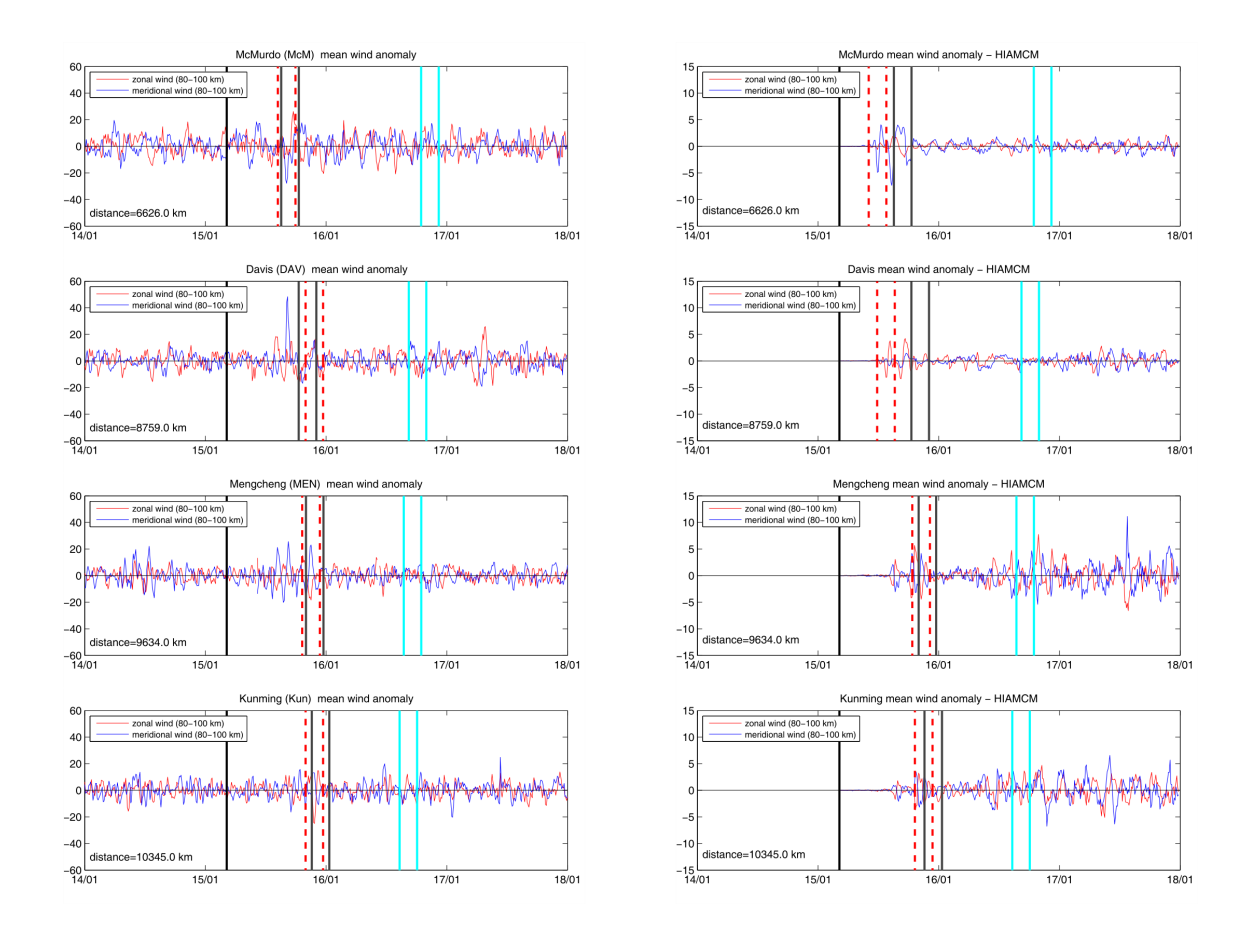


Figure 4. The same as Figure 3, but for the stations westward of HTHH outside the European continent.

180

of the eruption sequence. The spatial uncertainty is given by the diameter of the observation volume and we used 350 km for all stations.

Figure 6 shows four panels summarizing the analysis. The left column presents the meteor radar observations and the right column the HIAMCM data. The observational data can be grouped in an eastward wave (red line) with an observed phase speed of  $240 \pm 5.7$  m/s and a westward traveling GW (blue line) exhibiting an observed phase speed of  $166 \pm 6.4$  m/s. The fits were obtained by separating the stations according to their relative position (eastward or westward) of HTHH. The eastward stations of ROT, TDF, ALO, PKF, CMOR, CAR, COL, TRO, and SVA provide enough data to determine the eruption time to within 6-12 min and eruption location to be within 80 km of the nominal HTHH coordinates in the WGS84 reference. The precision of the fitting coefficients significantly depends on the European stations. Due to the much larger distance and time between the eruption, the errors of the individual measurements are less critical. The westward wave (blue) was analyzed using a regularized fit. The fit is regularized by a fixed eruption time t0 = 0 hours and by a fixed location using the nominal HTHH coordinate. This strategy is necessary to account for the much smaller number of observations. The relative distance between DAV, KUN, and MEN and the volcano is almost identical leaving essentially only McM as a second point. Thus, we added the

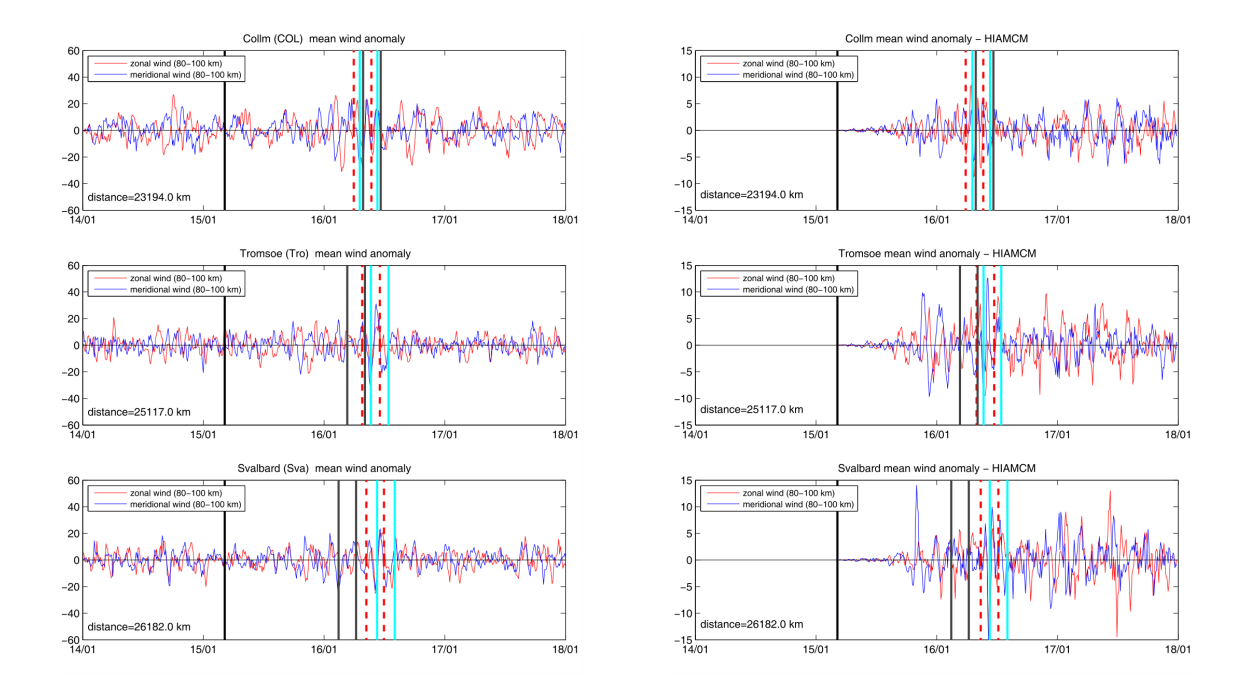


Figure 5. The same as Figure 3, but for the European meteor radar sites.

190

195

westward HTHH wave signature that was found in the ALO and already presented in Stober et al. (2023) to the fit.

The same analysis is applied to HIAMCM and the fitted observed phase velocities for the eastward and westward HTHH GW are in very good agreement between the model and the observations. Only the Antarctic stations of McM and DAV show a substantial deviation. Apparently, the Q2DW way plays an important role and is clearly visible in the southern hemisphere at mesospheric altitudes in the meteor radar data (Stober et al., 2023). However, there is no indication of this wave found in MERRA2 and, thus, due to the nudging of the large-scale dynamics in HIAMCM from the re-analysis, it is also missing in the HIAMCM winds. The amplitude of the Q2DW is strongest in the meridional wind component and showed a clear northward wind direction during the time of eruption above the South American continent. Climatological studies of the Q2DW have shown that the wavenumber 3 often dominates in the southern hemisphere around 30°S, which suggests that the HTHH GW-package faced a strong headwind towards the south (Iimura et al., 2021). This explains the different arrival times of the HTHH GW package at these stations and it also underlines why the signatures in McM and DAV are less clear, although these stations are closer to the eruption compared to many other meteor radars used in this study.

Finally, Figure 7 compares the derived observed phase speed for each station separately relative to the distance along the GC path for each radar (left panel) and HIAMCM (right panel). The ALO station is added with both detections of the HTHH GW and, thus, appears at two distances representing the eastward and westward GC distance. There is a remarkable agreement for some stations like ALO, SVA, TRO, CAR, COL, MEN, and KUN to within  $\pm 5$  m/s. Furthermore, this comparison reflects that we are able to identify two clusters that correspond to the eastward and westward HTHH GW package. It is also obvious that

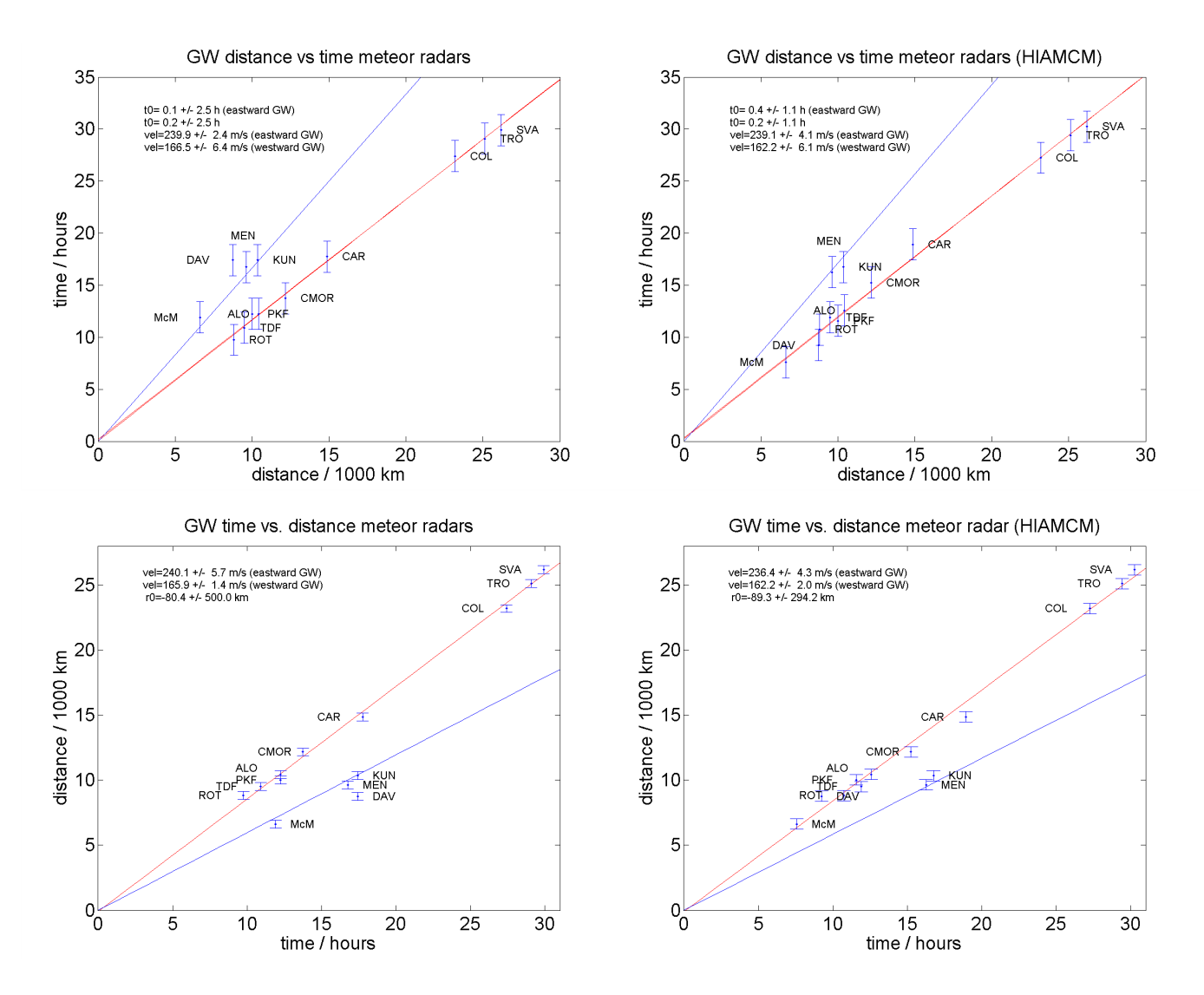


**Figure 6.** Gravity wave phase speed analysis for the meteor radars (left column) and HIAMCM (right column) as distance versa time and time versa distance plots. The red line indicates the best fit for the eastward propagating HTHH GW, the blue line is the best fit for the westward propagating HTHH GW.

the observed phase speed remains constant with distance from the volcano. The reasons for the exceptional behavior of DAV and McM in the HIAMCM data are already discussed.

### 6 Discussion

Although meteor radars have become a widely used sensor to observe mesospheric winds, there have been almost no studies on the HTHH eruption leveraging such observations. Identifying the HTHH GW in standard monostatic meteor radars turned

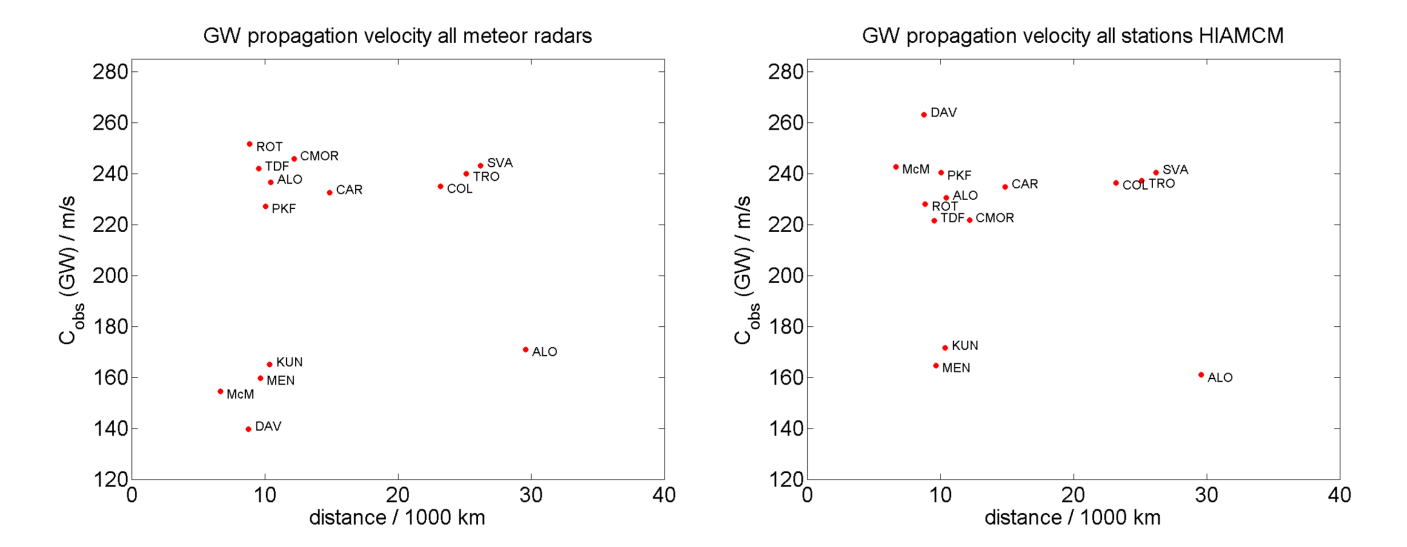


Figure 7. Comparison of individual observed phase velocities for the meteor radars and HIAMCM.

out to be more challenging than expected from the stratospheric data (Wright et al., 2022) and become only feasible due to the results obtained from the high-resolution analysis with the 3DVAR+DIV algorithm (Stober et al., 2023). HIAMCM simulations represent a much more fragmented wavefront for the volcanic-caused gravity waves with distinct azimuthal differences relative to the eruption site (Vadas et al., 2023a) compared to high-resolution WACCM-X data obtained for the pseudo-Lamb wave modes (Liu et al., 2023).

Many other publications emphasized the Lamb wave generated during the first eruption (Wright et al., 2022; Matoza et al., 2022), which was observable in surface pressure data and the brightness temperatures of infrared satellites. However, high-resolution wind measurements indicated only weak signatures of a possible Lamb wave at the MLT below 90 km altitude (Stober et al., 2023). Upon reaching the GW seeding altitude of z 110 km, the small-amplitude Lamb waves would likely have seeded a continuum spectrum of upward and downward-propagating GWs similar to the GWs excited by a localized ocean wave packet such as a tsunami (?). This is possibly the source of the enhanced GW activity before the HTHH eastward GW actually arrived in the observation volume (Stober et al., 2023). Similar observations can be made for the MEN and KUN meteor radars in China, which also reveal an increased variability before the westward HTHH GWs arrived.

The observed phase velocities derived in this study crucially depend on how the timing is determined and referenced. In the literature, typically the onset of the HTHH eruption sequence is used as a reference (15th January 04:15 UTC). However, this captures only partially the complexity of the eruption sequence, which lasted for about three hours and consisted of several vigorous explosions. We accounted for this complexity by always embracing the HTHH GW package by vertical lines where the left one refers to the onset and the right one is given by onset +3 hours. This is important for the comparison with HIAMCM where 5 primary volcanic eruptions are modeled with different launch times spread over 1 hour 30 min after the initial primary explosion (Vadas et al., 2023a). Furthermore, there is a longitudinal and meridional shift of the location of the updrafts from

GOES-17 of about 0.7° or about 70-90 km, and the nominal geographic coordinates of the volcano (175.38° W, 20.54° S), which we used as a reference to compute the distances. Considering these aspects underlines how precise the t0-time and also the location of the eruption have been inferred from the global meteor radar data.

230

240

250

255

A key factor for the propagation of the GWs is the speed of sound, which forms an effective natural altitude-dependent bottleneck or barrier. Since most of the large-amplitude secondary GWs were created at z 120-150 km (e.g., Fig. 13 of Vadas et al., 2023b), those that propagate through the MLT are downward-propagating. The mesopause region typically has a sound speed of cs 280 m/s, which results in a maximum intrinsic horizontal phase speed of 0.9cs 280 m/s (?)l. This is why the GWs observed in the MLT had a maximum of 240 m/s. In addition, the eruption occurred during the southern hemispheric summer, where temperatures below 140 K are expected and confirmed due to the presence of NLC in Tierra del Fuego. These temperatures for the lower southern latitudes around the Antarctic continent are consistent with a speed of sound limit close to approximately 239 m/s (Stober et al., 2023), which results in a maximum intrinsic horizontal phase speed of 0.9cs 215 m/s. This played an important role in why the MLT winds at DAV and McM did not show a large amplitude or clear wave pattern of the HTHH GW at both sites, although both stations are located at the closest distance to HTHH of all meteor radars included in our study. However, the HIAMCM predicted that McM and DAV would observe HTHH GWs with an observed phase velocity of about 240 m/s. As mentioned previously this wave was Doppler shifted due to a strong Q2DW activity in the southern hemisphere (Stober et al., 2023), which was also found in ROT, TDF, McM, and DAV (data not shown) and, thus, explains the differences in the arrival times between the observations and HIAMCM. However, it also confirms that the intrinsic wave speed was much closer to the sound speed barrier and, thus, forced the HTHH GW to reflect, thereby preventing the GW from entering the Antarctic polar MLT region. Hence, the HTHH GW signatures in the MLT winds presented in this study only show the lower height range of the HTHH GWs launched in this direction.

Comparing the observations from MEN, KUN, ALO, and CAR confirms findings presented in a previous study about the intrinsic wave properties of the HTHH GW traveling along the GC. All four stations are located rather close to the same GC and, thus, are suitable to evaluate the results obtained from the high-resolution 3DVAR+DIV retrievals (Stober et al., 2023). Hence, this study confirmed the intrinsic wave speed to be 202.5 m/s for this GC propagation. This velocity is low enough to not suffer from any speed of sound limitations due to a too-cold mesosphere somewhere along the GC, which is confined between 40° S and 40° N. This might also explain why only the 3DVAR+DIV analysis at CONDOR revealed both signs of the eastward and westward HTHH GW. Simulations of the Lamb wave modes L0 and L1 with WACCM-X suggest that the L1 has a phase speed of about 240 m/s (Liu et al., 2023). Although this phase speed seems to agree with the observed phase speeds in this study, the horizontal wavelength of about 1600-2000 km (Stober et al., 2023), and the wave period of 2 hours 20 min is far away from the properties presented in the simulations. Furthermore, HIAMCM and meteor radar zonal and meridional winds exhibit variable phase relations between both wind components and a much less coherent phase front than expected for a Lamb wave. There might have been a L1 mode in the MLT but it seems to be less visible in the available meteor radar wind data. The spatial averaging of 350 km in diameter and temporal resolution of 10 min clearly sets limits concerning this wave.

7 Conclusions

265

275

280

260 In this study, we analyzed winds from 13 globally distributed meteor radars to track the motion of the HTHH GW package

in the eastward and westward directions from the volcano. The observational data was compared to nudged simulations with

HIAMCM. We were able to identify the HTHH wave or its remnants in the observations and applied the same observational

filter to HIAMCM. We were able to track eastward propagating HTHH GWs over almost 30000 km from the eruption site in

the Pacific up to the Arctic over Svalbard. We determined an observed horizontal phase velocity of  $240\pm5.7$  m/s. Furthermore,

we found westward propagating HTHH GWs with an observed horizontal phase speed of  $166.5 \pm 6.4$  m/s. The observed phase

speeds are in excellent agreement with HIAMCM, which rendered observed phase speeds of 239.5±4.3 m/s and 162.2±6.1

m/s for the eastward and westward GWs, respectively.

The comparison between the meteor radar winds and HIAMCM underlines the ability of HIAMCM to model the HTHH GW

and their propagation over long distances when the model is nudged to reanalysis fields to prescribe the large-scale dynamics.

The HTHH eruption provided an ideal testbed to evaluate and compare observations and models to investigate GW dynamics

from a known and well-defined source throughout the atmosphere. Due to the unique thermal and dynamic conditions at the

MLT, HIAMCM revealed the much more complex structure of the wavefront generated by the HTHH eruption compared to

the observations shown at the stratosphere (Wright et al., 2022), which can be also found in the observations.

Tracking the eastward HTHH GW in the meteor radar winds permitted to determine the eruption time to be within 6 min of

the nominal eruption time (15th Jan 2022 04:15 UTC) and the location was found to be within a range of 78 km to the WGS84

coordinates of the volcano. Both values are in good agreement with HIAMCM and within derived statistical uncertainties.

Furthermore, the rather accurate, but not very precise, localization of the eruption location is consistent with HIAMCM and

other studies, in particular, when considering the complexity of the eruption sequence modeled with HIAMCM, which is based

on GOES-17 updrafts. These updrafts are extending over 0.7° in longitude and show a horizontal distance of up to 70 km from

the volcano WGS84 coordinates.

Author contributions. TEXT

Competing interests. TEXT

Disclaimer. Any opinions, findings, and conclusions or recommendations expressed in this material are those of the author(s) and do not

necessarily reflect the views of the National Science Foundation.

Acknowledgements. Gunter Stober, Witali Krochin and Guochun Shi are members of the Oeschger Center for Climate Change Research (OCCR). Witali Krochin and Guochun Shi are supported by the Schweizerischer Nationalfonds zur Förderung der Wissenschaftlichen Forschung (grant no. 200021-200517 / 1).

SLV and EB were supported by NSF grant # AGS-1832988.

300

no. 80NSSC21M0073.

The work by Alan Liu is supported by (while serving at) the National Science Foundation (NSF), USA. Zishun Qiao and the operation of the CONDOR meteor radar system is supported by the NSF grant 1828589.

The Esrange meteor radar operation, maintenance, and data collection were provided by the Esrange Space Center of the Swedish Space Corporation.

This research has been supported by the STFC (grant no. ST/W00089X/1 to Mark Lester).

This study is partly supported by Grants-in-Aid for Scientific Research (no. 17H02968) of the Japan Society for the Promotion of Science 295 (JSPS).

Njål Gulbrandsen acknowledges the support of the Leibniz Institute of Atmospheric Physics (IAP), Kühlungsborn, Germany for their contributions to the upgrade of the TRO meteor radar.

Support for DJ as well as SAAMER-OS' operation are provided by NASA's Planetary Science Division Research Program, through ISFM work package Exospheres, Ionospheres, Magnetospheres Modeling at Goddard Space Flight Center and NASA Engineering Saftey Center (NESC) assessment TI-17-01204. This work was supported in part by the NASA Meteoroid Environment Office under cooperative agreement

The work by Wen Yi is supported by the National Natural Science Foundation of China (grants No. 42174183).

## References

320

- Andrioli, V. F., Fritts, D. C., Batista, P. P., and Clemesha, B. R.: Improved analysis of all-sky meteor radar measurements of gravity wave variances and momentum fluxes, Annales Geophysicae, 31, 889–908, https://doi.org/10.5194/angeo-31-889-2013, 2013.
  - Becker, E. and Vadas, S. L.: Secondary Gravity Waves in the Winter Mesosphere: Results From a High-Resolution Global Circulation Model, Journal of Geophysical Research: Atmospheres, 123, 2605–2627, https://doi.org/10.1002/2017JD027460, 2018.
  - Becker, E. and Vadas, S. L.: Explicit Global Simulation of Gravity Waves in the Thermosphere, Journal of Geophysical Research: Space Physics, 125, e2020JA028 034, https://doi.org/10.1029/2020JA028034, e2020JA028034 10.1029/2020JA028034, 2020.
- Becker, E., Vadas, S. L., Bossert, K., Harvey, V. L., Zülicke, C., and Hoffmann, L.: A High-Resolution Whole-Atmosphere Model With Resolved Gravity Waves and Specified Large-Scale Dynamics in the Troposphere and Stratosphere, Journal of Geophysical Research: Atmospheres, 127, e2021JD035018, https://doi.org/https://doi.org/10.1029/2021JD035018, e2021JD035018, 2021.
  - Brown, P., Wong, D., Weryk, R., and Wiegert, P.: A meteoroid stream survey using the Canadian Meteor Orbit Radar: II: Identification of minor showers using a 3D wavelet transform, Icarus, 207, 66–81, https://doi.org/https://doi.org/10.1016/j.icarus.2009.11.015, 2010.
- 315 Carr, J. L., Horváth, A., Wu, D. L., and Friberg, M. D.: Stereo Plume Height and Motion Retrievals for the Record-Setting Hunga Tonga-Hunga Ha'apai Eruption of 15 January 2022, Geophysical Research Letters, 49, e2022GL098131, https://doi.org/https://doi.org/10.1029/2022GL098131, e2022GL098131 2022GL098131, 2022.
  - Dempsey, S. M., Hindley, N. P., Moffat-Griffin, T., Wright, C. J., Smith, A. K., Du, J., and Mitchell, N. J.: Winds and tides of the Antarctic mesosphere and lower thermosphere: One year of meteor-radar observations over Rothera (68°S, 68°W) and comparisons with WACCM and eCMAM, Journal of Atmospheric and Solar-Terrestrial Physics, 212, 105510, https://doi.org/10.1016/j.jastp.2020.105510, 2021.
  - Fritts, D. C., Janches, D., Iimura, H., Hocking, W. K., Mitchell, N. J., Stockwell, R. G., Fuller, B., Vandepeer, B., Hormaechea, J., Brunini, C., and Levato, H.: Southern Argentina Agile Meteor Radar: System design and initial measurements of large-scale winds and tides, Journal of Geophysical Research: Atmospheres, 115, https://doi.org/10.1029/2010JD013850, 2010.
- Gudadze, N., Stober, G., and Chau, J. L.: Can VHF radars at polar latitudes measure mean vertical winds in the presence of PMSE?, Atmospheric Chemistry and Physics, 19, 4485–4497, https://doi.org/10.5194/acp-19-4485-2019, 2019.
  - Hall, C. and Tsutsumi, M.: Neutral temperatures at 90 km altitude over Svalbard (78°N 16°E), 2002–2019, derived from meteor radar observations, Polar Science, 24, 100 530, https://doi.org/10.1016/j.polar.2020.100530, 2020.
- Hall, C. M. and Tsutsumi, M.: Changes in mesospheric dynamics at 78°N, 16°E and 70°N, 19°E: 2001–2012, Journal of Geophysical Research: Atmospheres, 118, 2689 2701, 2013.
  - Heki, K.: Ionospheric signatures of repeated passages of atmospheric waves by the 2022 Jan. 15 Hunga Tonga-Hunga Ha'apai eruption detected by QZSS-TEC observations in Japan, Earth, Planets and Space, 74, https://doi.org/10.1186/s40623-022-01674-7, 2022.
  - Hocking, W., Fuller, B., and Vandepeer, B.: Real-time determination of meteor-related parameters utilizing modern digital technology, Journal of Atmospheric and Solar-Terrestrial Physics, 63, 155 169, https://doi.org/http://dx.doi.org/10.1016/S1364-6826(00)00138-3, radar applications for atmosphere and ionosphere research PIERS 1999, 2001.
  - Hocking, W. K., Thayaparan, T., and Jones, J.: Meteor decay times and their use in determining a diagnostic mesospheric Temperature-pressure parameter: Methodology and one year of data, Geophysical Research Letters, 24, 2977–2980, https://doi.org/10.1029/97GL03048, 1997.

- Holdsworth, D. A., Reid, I. M., and Cervera, M. A.: Buckland Park all-sky interferometric meteor radar, Radio Science, 39, n/a–n/a, https://doi.org/10.1029/2003RS003014, rS5009, 2004.
  - Iimura, H., Fritts, D. C., Lieberman, R. S., Janches, D., Mitchell, N. J., Franke, S. J., Singer, W., Hocking, W. K., Taylor, M. J., and Moffat-Griffin, T.: Climatology of quasi-2-day wave structure and variability at middle latitudes in the northern and southern hemispheres, Journal of Atmospheric and Solar-Terrestrial Physics, 221, 105 690, https://doi.org/https://doi.org/10.1016/j.jastp.2021.105690, 2021.
- Jacobi, C., Fröhlich, K., Viehweg, C., Stober, G., and Kürschner, D.: Midlatitude mesosphere/lower thermosphere meridional winds and temperatures measured with meteor radar, Advances in Space Research, 39, 1278–1283, https://doi.org/https://doi.org/10.1016/j.asr.2007.01.003, 2007.
  - Liu, H.-L., Wang, W., Huba, J. D., Lauritzen, P. H., and Vitt, F.: Atmospheric and Ionospheric Responses to Hunga-Tonga Volcano Eruption Simulated by WACCM-X, Geophysical Research Letters, 50, e2023GL103682, https://doi.org/https://doi.org/10.1029/2023GL103682, e2023GL103682, 2023GL103682, 2023.
- Marino, J., Palo, S. E., and Rainville, N.: First Observations From a New Meteor Radar at McMurdo Station Antarctica (77.8°S, 166.7°E), Radio Science, 57, e2022RS007466, https://doi.org/https://doi.org/10.1029/2022RS007466, e2022RS007466 2022RS007466, 2022.
  - Matoza, R. S., Fee, D., Assink, J. D., Iezzi, A. M., Green, D. N., Kim, K., Toney, L., Lecocq, T., Krishnamoorthy, S., Lalande, J.-M., Nishida, K., Gee, K. L., Haney, M. M., Ortiz, H. D., Brissaud, Q., Martire, L., Rolland, L., Vergados, P., Nippress, A., Park, J., Shani-Kadmiel, S., Witsil, A., Arrowsmith, S., Caudron, C., Watada, S., Perttu, A. B., Taisne, B., Mialle, P., Pichon, A. L., Vergoz, J., Hupe, P., Blom, P. S.,
- Waxler, R., Angelis, S. D., Snively, J. B., Ringler, A. T., Anthony, R. E., Jolly, A. D., Kilgour, G., Averbuch, G., Ripepe, M., Ichihara, M., Arciniega-Ceballos, A., Astafyeva, E., Ceranna, L., Cevuard, S., Che, I.-Y., Negri, R. D., Ebeling, C. W., Evers, L. G., Franco-Marin, L. E., Gabrielson, T. B., Hafner, K., Harrison, R. G., Komjathy, A., Lacanna, G., Lyons, J., Macpherson, K. A., Marchetti, E., McKee, K. F., Mellors, R. J., Mendo-Pérez, G., Mikesell, T. D., Munaibari, E., Oyola-Merced, M., Park, I., Pilger, C., Ramos, C., Ruiz, M. C., Sabatini, R., Schwaiger, H. F., Tailpied, D., Talmadge, C., Vidot, J., Webster, J., and Wilson, D. C.: Atmospheric waves and global seismoacoustic

observations of the January 2022 Hunga eruption, Tonga, Science, 377, 95–100, https://doi.org/10.1126/science.abo7063, 2022.

360

365

370

- Meek, C. E., Manson, A. H., Hocking, W. K., and Drummond, J. R.: Eureka, 80°N, SKiYMET meteor radar temperatures compared with Aura MLS values, Annales Geophysicae, 31, 1267–1277, https://doi.org/10.5194/angeo-31-1267-2013, 2013.
- Millán, L., Santee, M. L., Lambert, A., Livesey, N. J., Werner, F., Schwartz, M. J., Pumphrey, H. C., Manney, G. L., Wang, Y., Su, H., Wu, L., Read, W. G., and Froidevaux, L.: The Hunga Tonga-Hunga Ha'apai Hydration of the Stratosphere, Geophysical Research Letters, 49, e2022GL099381, https://doi.org/10.1029/2022GL099381, e2022GL099381, 2022GL099381, 2022.
- Miyoshi, Y. and Shinagawa, H.: Upward propagation of gravity waves and ionospheric perturbations triggered by the 2022 Hunga-Tonga volcanic eruption, Earth Planets Space, 75, https://doi.org/doi.org/10.1186/s40623-023-01827-2, 2023.
- National Imagery and Mapping Agency: Department of Defense World Geodetic System 1984: its definition and relationships with local geodetic systems, Tech. Rep. TR8350.2, National Imagery and Mapping Agency, St. Louis, MO, USA, http://earth-info.nga.mil/GandG/publications/tr8350.2/tr8350\_2.html, 2000.
- Pokhotelov, D., Becker, E., Stober, G., and Chau, J. L.: Seasonal variability of atmospheric tides in the mesosphere and lower thermosphere: meteor radar data and simulations, Annales Geophysicae, 36, 825–830, https://doi.org/10.5194/angeo-36-825-2018, 2018.
- Shinbori, A., Otsuka, Y., Sori, T., Nishioka, M., Perwitasari, S., Tsuda, T., and Nishitani, N.: Electromagnetic conjugacy of ionospheric disturbances after the 2022 Hunga Tonga-Hunga Ha'apai volcanic eruption as seen in GNSS-TEC and SuperDARN Hokkaido pair of radars, Earth, Planets and Space, 74, https://doi.org/10.1186/s40623-022-01665-8, 2022.

- Stober, G., Baumgarten, K., McCormack, J. P., Brown, P., and Czarnecki, J.: Comparative study between ground-based observations and NAVGEM-HA analysis data in the mesosphere and lower thermosphere region, Atmospheric Chemistry and Physics, 20, 11 979–12 010, https://doi.org/10.5194/acp-20-11979-2020, 2020.
- Stober, G., Janches, D., Matthias, V., Fritts, D., Marino, J., Moffat-Griffin, T., Baumgarten, K., Lee, W., Murphy, D., Kim, Y. H., Mitchell, N., and Palo, S.: Seasonal evolution of winds, atmospheric tides, and Reynolds stress components in the Southern Hemisphere mesosphere—lower thermosphere in 2019, Annales Geophysicae, 39, 1–29, https://doi.org/10.5194/angeo-39-1-2021, 2021a.
  - Stober, G., Kozlovsky, A., Liu, A., Qiao, Z., Tsutsumi, M., Hall, C., Nozawa, S., Lester, M., Belova, E., Kero, J., Espy, P. J., Hibbins, R. E., and Mitchell, N.: Atmospheric tomography using the Nordic Meteor Radar Cluster and Chilean Observation Network De Meteor Radars: network details and 3D-Var retrieval, Atmospheric Measurement Techniques, 14, 6509–6532, https://doi.org/10.5194/amt-14-6509-2021, 2021b.

400

- Stober, G., Kuchar, A., Pokhotelov, D., Liu, H., Liu, H.-L., Schmidt, H., Jacobi, C., Baumgarten, K., Brown, P., Janches, D., Murphy, D., Kozlovsky, A., Lester, M., Belova, E., Kero, J., and Mitchell, N.: Interhemispheric differences of mesosphere–lower thermosphere winds and tides investigated from three whole-atmosphere models and meteor radar observations, Atmospheric Chemistry and Physics, 21, 13 855–13 902, https://doi.org/10.5194/acp-21-13855-2021, 2021c.
- Stober, G., Liu, A., Kozlovsky, A., Qiao, Z., Kuchar, A., Jacobi, C., Meek, C., Janches, D., Liu, G., Tsutsumi, M., Gulbrandsen, N., Nozawa, S., Lester, M., Belova, E., Kero, J., and Mitchell, N.: Meteor radar vertical wind observation biases and mathematical debiasing strategies including the 3DVAR+DIV algorithm, Atmospheric Measurement Techniques, 15, 5769–5792, https://doi.org/10.5194/amt-15-5769-2022, 2022.
- Stober, G., Liu, A., Kozlovsky, A., Qiao, Z., Krochin, W., Shi, G., Kero, J., Tsutsumi, M., Gulbrandsen, N., Nozawa, S., Lester, M., Baumgarten, K., Belova, E., and Mitchell, N.: Identifying gravity waves launched by the Hunga Tonga–Hunga Ha'apai volcanic eruption in mesosphere/lower-thermosphere winds derived from CONDOR and the Nordic Meteor Radar Cluster, Annales Geophysicae, 41, 197–208, https://doi.org/10.5194/angeo-41-197-2023, 2023.
  - Themens, D. R., Watson, C., Žagar, N., Vasylkevych, S., Elvidge, S., McCaffrey, A., Prikryl, P., Reid, B., Wood, A., and Jayachandran, P. T.: Global Propagation of Ionospheric Disturbances Associated With the 2022 Tonga Volcanic Eruption, Geophysical Research Letters, 49, e2022GL098158, https://doi.org/https://doi.org/10.1029/2022GL098158, e2022GL098158 2022GL098158, 2022.
  - Vadas, S. L. and Becker, E.: Numerical Modeling of the Excitation, Propagation, and Dissipation of Primary and Secondary Gravity Waves during Wintertime at McMurdo Station in the Antarctic, Journal of Geophysical Research: Atmospheres, 123, 9326–9369, https://doi.org/10.1029/2017JD027974, 2018.
- Vadas, S. L., Becker, E., Figueiredo, C., Bossert, K., Harding, B. J., and Gasque, L. C.: Primary and Secondary Gravity Waves and Large-Scale Wind Changes Generated by the Tonga Volcanic Eruption on 15 January 2022: Modeling and Comparison With ICON-MIGHTI Winds, Journal of Geophysical Research: Space Physics, 128, e2022JA031138, https://doi.org/https://doi.org/10.1029/2022JA031138, e2022JA031138 2022JA031138, 2023a.
  - Vadas, S. L., Figueiredo, C., Becker, E., Huba, J. D., Themens, D. R., Hindley, N. P., Mrak, S., Galkin, I., and Bossert, K.: Traveling ionospheric disturbances induced by the secondary gravity waves from the Tonga eruption on 15 January 2022: Modeling with MESO-RAC/HIAMCM/SAMI3 and comparison with GPS/TEC and ionosonde data, Journal of Geophysical Research: Space Physics, n/a, e2023JA031408, https://doi.org/l0i.org/10.1029/2023JA031408, e2023JA031408 2023JA031408, 2023b.
  - Webster, A. R., Brown, P. G., Jones, J., Ellis, K. J., and Campbell-Brown, M.: Canadian Meteor Orbit Radar (CMOR), Atmospheric Chemistry and Physics, 4, 679–684, https://doi.org/10.5194/acp-4-679-2004, 2004.

- Wright, C. J., Hindley, N. P., Alexander, M. J., Barlow, M., Hoffmann, L., Mitchell, C. N., Prata, F., Bouillon, M. and Carstens, J., Clerbaux,
- 415 C., Osprey, S. M., Powell, N., Randall, C. E., and Yue, J.: Surface-to-space atmospheric waves from Hunga Tonga-Hunga Ha'apai eruption, Nature, 609, 741–746, https://doi.org/https://doi.org/10.1038/s41586-022-05012-5, 2022.
  - Yamada, M., Ho, T.-C., Mori, J., Nishikawa, Y., and Yamamoto, M.-Y.: Tsunami Triggered by the Lamb Wave From the 2022 Tonga Volcanic Eruption and Transition in the Offshore Japan Region, Geophysical Research Letters, 49, e2022GL098752, https://doi.org/10.1029/2022GL098752, e2022GL098752 2022GL098752, 2022.
- 420 Yang, C., Lai, D., Yi, W., Wu, J., Xue, X., Li, T., Chen, T., and Dou, X.: Observed Quasi 16-Day Wave by Meteor Radar over 9 Years at Mengcheng (33.4° N, 116.5°E) and Comparison with the Whole Atmosphere Community Climate Model Simulation, Remote Sensing, 15, https://doi.org/10.3390/rs15030830, 2023.
  - Zeng, J., Yi, W., Xue, X., Reid, I., Hao, X., Li, N., Chen, J., Chen, T., and Dou, X.: Comparison between the Mesospheric Winds Observed by Two Collocated Meteor Radars at Low Latitudes, Remote Sensing, 14, https://doi.org/10.3390/rs14102354, 2022.
- Zhang, S.-R., Vierinen, J., Aa, E., Goncharenko, L. P., Erickson, P. J., Rideout, W., Coster, A. J., and Spicher, A.: 2022 Tonga volcanic eruption induced global propagation of ionospheric disturbances via Lamb waves, 2022.